Title: Mechanical Nanolattice Printed Using Nanocluster-Based Photoresist

Authors: Qi Li[1#]*, John Kulikowski[1#], David Doan[1#], Ottman A. Tertuliano[1], Charles J. Zeman IV[2], Melody M Wang,[1] George C. Schatz,[2] X. Wendy Gu[1]*

Affiliations:

[1]Department of Mechanical Engineering, Stanford University; Stanford, CA, 94305 USA.

[2]Department of Chemistry, Northwestern University, Evanston, Illinois 60208, USA.

*Corresponding authors. Email: qilistan@stanford.edu and xwgu@stanford.edu

[#] These authors contributed equally to this work.

Abstract: Natural materials exhibit emergent mechanical properties due to their nanoarchitected, nanocomposite structures. Fabrication of such complex structures is challenging because state-of-the-art 3D nanoprinting is mostly based on organic photoresists and limited to simple, homogenous materials. Here we report a strategy for the rapid nanoprinting of various inorganic-organic nanocomposites using metal nanoclusters, which function as highly sensitive two-photon initiators, acid generators, sensitizers, and simultaneously serve as inorganic precursors for mechanical reinforcements and nanoscale porogens. We demonstrate the printing of various nanocomposites with disparate nanoarchitectures, and structures with tunable, hierarchical and anisotropic nanoporosity. The printed nanocluster composite nanolattices exhibit high specific strength and energy absorption with good recoverability, stemming from material nonlinearities that produce significant hardening at large strains. This framework provides a generalizable approach for photoactive nanomaterials as versatile and transformative precursors in additive manufacturing of complex 3D lattices with emergent mechanical properties.

One-sentence summary: Nanocluster-based photoresists enable 3D printing of nanocomposite nanolattice with mechanical performance beyond conventional regimes.

Main Text: Advances in 3D printing (*i.e.,* additive manufacturing) rely on the invention of new printing techniques (*1–5*) and the creation of compatible feedstock materials such as resins, filaments, powders and photoresists (*6–9*). A current frontier is the printing of metals, ceramics and composites with arbitrary 3D nano- or micro-architectures (or lattices). These structures are of interest as next-generation mechanical metamaterials (*10*, *11*) that combine nanoscale material size effects with lightweight structural architectures, which leads to optimized strength, stiffness, or energy absorption per weight (*9–16*), as well as micro batteries, catalyst scaffolds and electromechanical devices (*17*, *18*). Improved performance and additional functionality could be achieved by printing advanced materials with complex internal nanofeatures, such as nanocomposites with optimized spacing and interactions between inorganic and organic components, or the hierarchical, graded porosity and structural anisotropy of natural structural materials (*19*). Fabrication of these complex nanostructures is currently limited by printing technique and appropriate feedstock.

Two-photon (or multiphoton) lithography (*4*, *20*) can achieve organic and a few hybrid (*21*) polymeric 3D nanostructures with almost arbitrary shape, but it remains challenging to print complex composite nanostructures as observed in natural materials (*10*, *17*). Two-photon lithography photoresists generally use photoinitiators that absorb two near-infrared photons to form radicals that initiate the polymerization of monomers (*22–26*). Currently, almost all two-photon initiators are organic molecules that do not enhance the properties of the final printed products (*22*, *26*). Composite structures can be printed by adding metal ions or inorganic particles to existing two-photon resists (*27–29*). However, these strategies are more used to print simple, functional structures (e.g., conductive wires, optical patterns, magnetic motors, etc.) (*18*), rather than the sophisticated, mechanical nanolattices because of the high flaw population and the reduced printability induced by the interference of particles with the propagating light and the laser-induced uncontrollable particle growth and aggregation (*10*, *30*). And due to the lack of high-quality, nanocomposite nanolattices being fabricated, so far it remains largely unknown how the nanofillers affect the mechanical behavior of the 3D lightweight ($\rho < 1 g/cm^3$) nanolattice. On the other hand, in recent years composite nanolattices with impressive mechanical performance were obtained by coating an inorganic layer onto a printed polymeric scaffold (*10*, *30–37*). However, this two-step strategy costs more fabrication time and only results in core-shell structures which limit the further optimization of mechanical performance.

Currently, many nanolattice materials show the post-yield softening or collapse (*33*) due to ……which limit…. and preclude their applications in ,,,,,,.

Here, we report the development of nanocluster-based photoresists that address these issues. In the past decade, ultrasmall metal nanoclusters of 1-2 nm in size have been synthesized with precise atomic structures (*38*). Compared to larger nanoparticles and smaller molecules, nanoclusters show distinct photochemical and photophysical properties (*38*), and we envision that nanoclusters could function as efficient, multifunctional two-photon activators (to be discussed). On the other hand, metal nanoclusters (1-2 nm) avoid the high energy requirement for metal ion reduction, and circumvent the light scattering that would occur with larger metal particles. Therefore, by using ultrasmall nanoclusters that replace traditional organic molecules as photoinitiators and substitute for metal ions or particles as inorganic precursors, we achieve the fast printing speeds with high structural precision, shape fidelity and geometric complexity.

We demonstrate that the nanocluster-based photoresists can be used to print disparate classes of composites that consist of metal nanoclusters embedded in polymers, glassy carbon and proteins. Nanocluster composite pillars and lattices are found to have a unique nonlinear stress-strain curve that shows increasing stiffness at large strains, as well as high specific strength and energy absorption beyond conventional regimes. These effects are specific to our nanocluster-based photoresist, and achieved through fewer processing steps than previous strategies to optimize mechanical metamaterials such as the addition of an inorganic coating to a polymeric scaffold (*31*).

The unique physical and chemical properties of metal nanoclusters enable the 3D printing of glassy carbon and protein lattices with hierarchical porosity down to ~10 nm. 3D printed nanocluster composites are converted into hierarchical and tunable nanoporous glassy carbon under pyrolysis. This derived structure forms through the melting of the nanoclusters, which occurs at 600-900^{o}C (*39*). The significant photothermal and photosensitization effect of metal nanoclusters (*40*) enables the 3D printing of silk fibroin lattices with anisotropic porosity and aligned nanocrystalline domains. These complex internal structures mimic the hierarchical porosity and structural anisotropy and gradience of natural structural materials such as bone (*19*), and they are currently inaccessible in 3D nanoprinting using traditional photoresists.

Results and Discussions

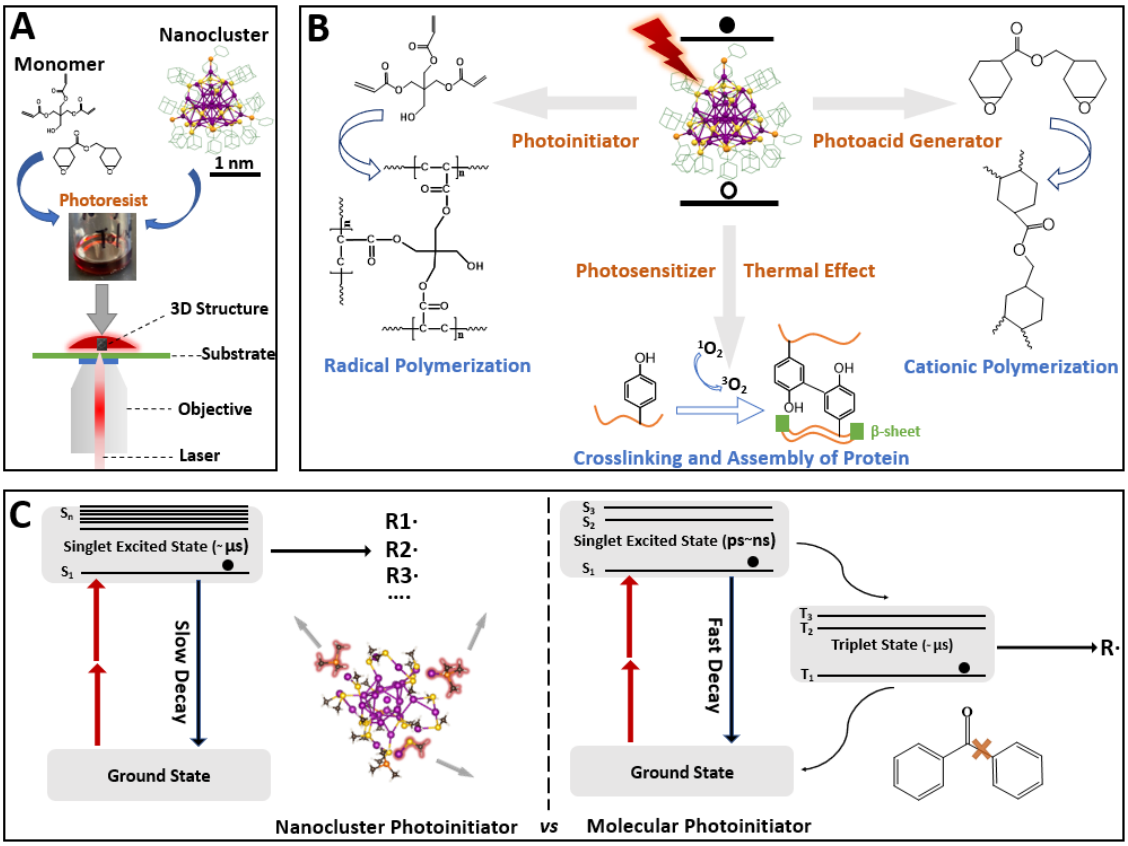

Fig. 1. Chemistry of Nanocluster-Based Photoresist. (**A**) Photoresist composition and printing setup. (**B**) Schematic of the photopolymerization of different types of monomers during two-photon lithography. The atomic structure of the nanocluster ($Ag_{28}Pt$) is reproduced from ref (*41*). **(C)** Comparison of the underlying photochemistry of nanocluster initiators (left) with typical organic initiators (right). The inset of (C) left shows a snapshot from excited-state Born-Oppenheimer molecular dynamics of $Ag_{28}Pt$, showing diverse fragmentation pathways.

Our nanocluster-based photoresist only consists of metal nanoclusters and monomers (*e.g.,* acrylate monomer such as pentaerythritol triacrylate (PETA), or epoxy monomer such as 3,4-epoxycyclohexylmethyl 3,4-epoxycyclohexanecarboxylate (EEC)) (Fig. 1A). Photoresists above 5 wt% nanoclusters were mixed with 2-propanol to combine the nanoclusters with monomers. As shown in Fig. 1B, nanoclusters can be used as photoinitiators for radical polymerization, and as photoacid generators for cationic polymerization, as well as the photosensitizers to promote singlet oxygen formation that induces the crosslinking of proteins. The $Ag_{28}Pt$ nanocluster (*41*) and the rod-shaped Au_{25} nanocluster (*42*) were selected as the two-photon initiators in this study, due to their high two-photon absorption cross-section, suitable photochemical characteristics, solubility in monomers, and stability under fabrication conditions. The 2PA cross-sections of $Ag_{28}Pt$ and Au_{25} were found to be >30 GM and >100 GM at sub-800 nm wavelengths,

respectively, as determined by quadratic response TDDFT calculations (Fig. S1). Time-dependent DFT calculations also found that two-photon absorption in these nanoclusters excite into a high density-of-states with metallic character, allowing for higher efficiency multiphoton absorption. Furthermore, these two nanoclusters show relatively low luminescent quantum yield (~5%) with slow radiative and non-radiative decay, such stable, long-living S_1 excited states (lifetime ~3 us) are beneficial for the generation of radicals or other reactive species (Fig. 1C, left). This is different than organic initiators in which the S_1 state is short-lived (ps-ns), and it is generally considered that the intersystem crossing to triplet states are needed for the generation of reactive species (*22*, *26*), which however, may reduce the overall photoinitiation efficiency of organic initiators. Furthermore, compared to molecule photoinitiators that usually only have a single, or very limited fragmentation pathways, nanoclusters provide for a much greater variety of bond scissions. Born-Oppenheimer molecular dynamics simulations on S_1 for $Ag_{28}Pt$ and Au_{25} show a wide range of ligand-dissociation mechanisms and fragment products, which ultimately lead to a greater range of reactivity with different reagents.

The printability of nanocluster-acrylate photoresist was systematically evaluated (Fig. 2). Squares and lines were fabricated as test structures to investigate the required scanning speed, threshold laser power, and minimal feature size of the nanocluster-acrylate photoresist. For the 5 wt% $Ag_{28}Pt$ photoresist (5 mg $Ag_{28}Pt$ nanoclusters and 95 mg PETA), laser powers from 2 to 30 mW and scanning speeds from 5 to 100 mm/s were evaluated (Fig. S2 and S3 show images of the fabricated square arrays). As shown in Fig. 2A, structures can be fabricated at relatively low applied powers of 4 mW and high speeds up to 100 mm/s. The fabricated structure shows photoluminescence (inset of Fig. S4) with a maximum peak at 720 nm, similar to $Ag_{28}Pt$ nanoclusters in solution, which suggests that the nanoclusters remain intact in the printed structure. Lines were fabricated (Fig. S5) and an x-y resolution of ~200-250 nm can be achieved. Au_{25} photoresists were also tested (Fig. 2B) which show similar performance with threshold power down to 2.5 mW and scanning speed up to 150 mm/s. Fig. 2 C-H show open-faced table, octet and Schwarz Primitive (SP) lattices written with high shape fidelity using the $Ag_{28}Pt$ and Au_{25} photoresist. As shown in Fig. 2D, freestanding 3D features can be as small as 400 nm. The minimal strut thicknesses of octet lattice structure (Fig. 2F) is 1.27 μm and the minimal wall thicknesses of SP lattices is 850 nm (Fig. 2H). Both Au_{25} and $Ag_{28}Pt$ nanoclusters can also function as two-photon acid generators for cationic polymerization of epoxy monomers (EEC)

with scanning speed up to 100 mm/s (laser power from ~25 to 35 mw) and the printed 3D structures are shown in Fig. S6.

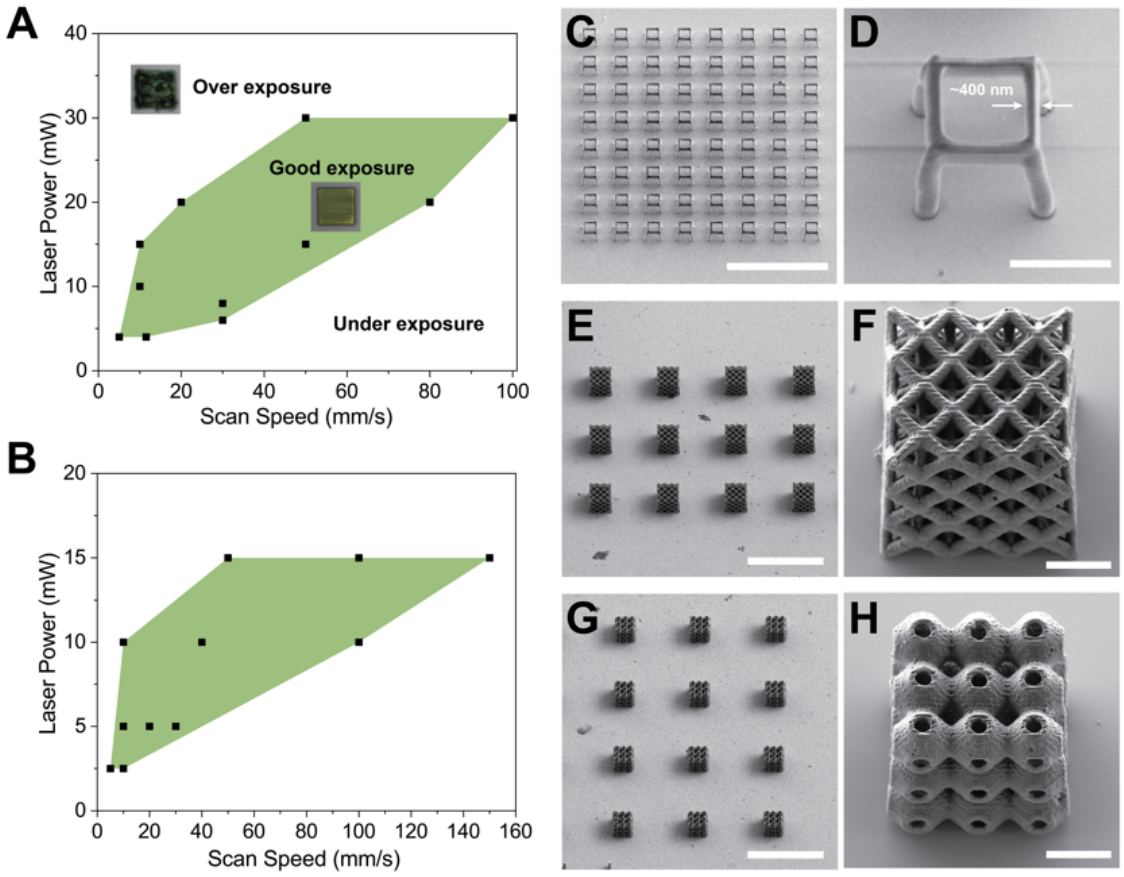

Fig. 2. Printability of Nanocluster-Based Photoresist. **(A)** and **(B)** Squares fabricated under different laser powers and scanning speed using 5 wt% $Ag_{28}Pt$ photoresist and 8 wt% Au_{25} photoresist. Insets are optical images of a square at two conditions: optimal exposure and over exposure. (**C**) and (**D**) Open-faced table fabricated using 5 wt% $Ag_{28}Pt$ photoresist. (**E**) and (**F**) Octet lattice made with 8 wt% Au_{25} photoresists. (**G**) and (**H**) Schwarz Primitive (SP) lattice made with 8 wt% Au_{25} photoresists.

The performance of the nanoclusters can be compared to other two-photon photoinitiators using a dimensionless figure-of-merit (FOM), where $FOM = vP_{th}^{-2}\lambda_0^3 R_p t_p (NA)^{-3}$ (*22*). Here, v is the scanning speed, P_{th} is the threshold laser power, λ_0 is the laser wavelength, R_p is the pulse repetition, and t_p is the pulse duration. NA is the numerical aperture of the objective lenses. The FOM of our nanocluster-PETA photoresist systems is greater than 10^2 with velocities up to 100 mm/s. Kiefer *et al*. reports that only six organic photoresist systems have a FOM $\geq 10^2$ at velocities $\geq$ 10 mm/s (Fig. S7) (*22*). It should be noted that Kiefer's FOM doesn't include the concentration of photoinitiators. Our nanocluster-based photoresists can fabricate good structures

using nanoclusters initiators of low mass percentage down to 0.4-2 wt% (dependent on the different batch of sample and the printer condition). Considering the molecular weight of the $Ag_{28}Pt$ and Au_{25} nanocluster is as high as 7275 and 7922 (*41*), the "dosage" of our nanocluster photoinitiator can be as small as 0.5-2.8 μmol/g in the resin; which is among the lowest values compared with hundreds of organic two-photon initiators(*26*). Overall, the Au_{25} and $Ag_{28}Pt$ nanoclusters show state-of-the-art performance comparable to the most efficient organic two-photon initiators (*22*), and furthermore, they can trigger the polymerization of more types of monomers, all under a high laser scanning speed, by way of diverse fragmentation pathways observed from molecular dynamics, leading to efficient nanoprinting of various nanocomposite structures.

We tested the mechanical behaviors of the nanocluster composite nanolattices (Fig. 3). The 10 wt% $Ag_{28}Pt$ PETA photoresist is used to fabricate honeycomb structures (Fig. 3A and C). The honeycombs have a height of 8.2 ± 0.1 μm, cell side length of 2.6 ± 0.2 μm, and wall thickness of 800 ± 50 nm. This results in a density of 0.58 g/cm^3 and relative density of ~48%. The compressive stress-strain response shows a linear region followed by a distinct yielding event at 35.3 ± 6.2 MPa. (Fig. 3B) After this, the stress-strain curve shows a nonlinear loading curve with a significant hardening at large strains until ultimate failure at ~25% strain. The honeycombs have a nominal failure stress of 178 ± 52 MPa. Comparatively, the literature has shown Ip-Dip honeycombs which yields and does not have any increase in stress beyond the yield point (*33*). We plot this along with our stress-strain curve in Fig 3B. Notably, our structure continues to increase in stress beyond the yield point, ultimately producing a structure with ultimately far better strength and energy absorption compared to the commercial Ip-Dip.

The 8 wt% Au_{25} PETA photoresist was used to fabricate cylindrical pillars of 2.5 μm in radius and 10 μm in height (Fig. S8). The mechanical properties of these pillars are evaluated with in-situ SEM compression testing. Small strain tests are used to determine the elastic modulus on the unloading curve. High strain tests are used to determine the ultimate compressive strength and failure mechanism. Cyclic tests evaluate the recoverability and energy dissipation properties of the photoresist. Engineering stress-strain curves also show a nonlinear loading curve with a significant hardening at large strain (Fig. S8). The elastic modulus was found to be 3.7 ± 0.2 GPa from the initial portion of the unloading curve (Fig.S9). Cyclic test shows 70% recovery for samples that were loaded to 30% strain (Fig. 10). For samples that were loaded to

failure, sudden failure occurs at 1.2 ± 0.1 GPa (Fig. S8**)**. This high strength and stiffness, coupled with the hyperelastic-like stress-strain response, leads to an energy absorption of 110 ± 50 MJ/m^3 (92 ± 42 kJ/kg) before initial crack formation.

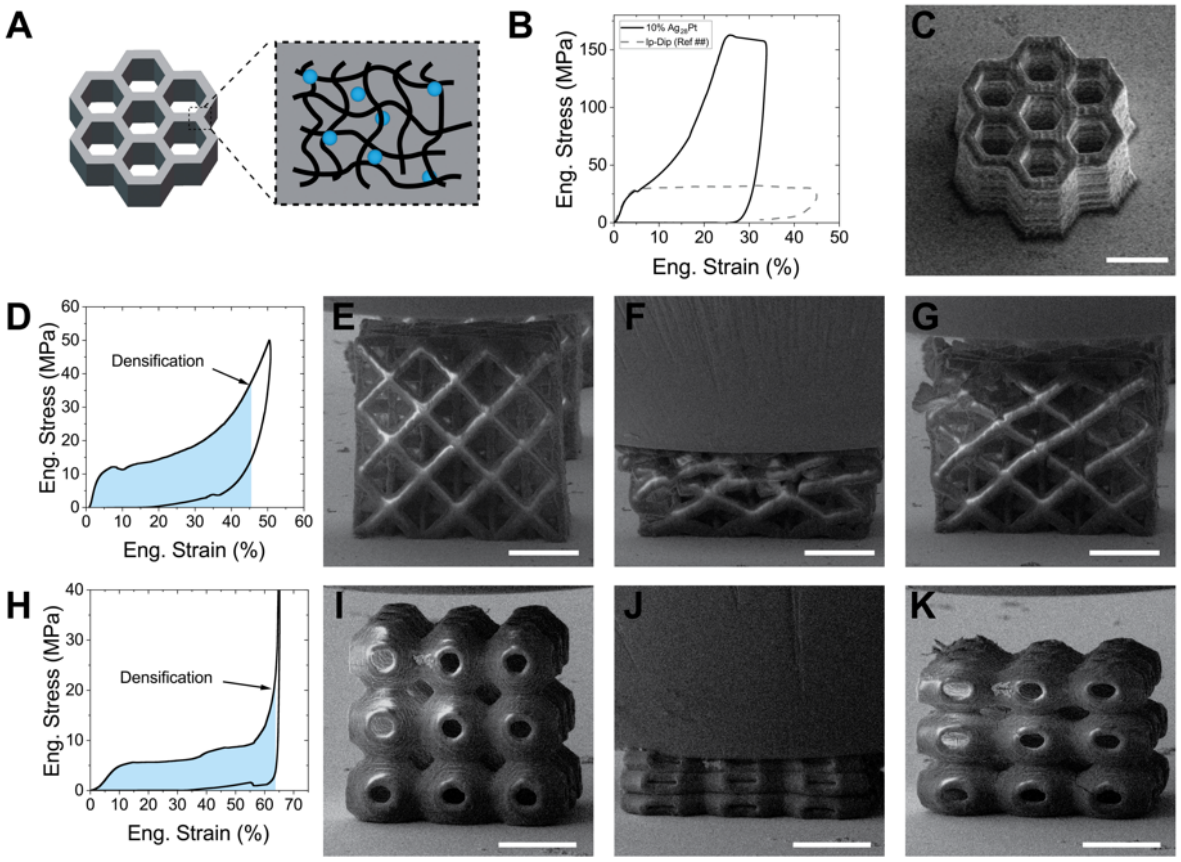

Fig. 3. Mechanical Behavior of Nanocluster Polymer Nanolattice. (**A**) Schematic of the nanocluster polymer nanolattice. (**B**) Engineering Stress-Engineering Strain Curve for honeycomb fabricated with 10wt% $Ag_{28}Pt$ photoresist. (**C**) SEM image of the honeycomb. (**D**) Engineering Stress-Engineering Strain curve for octet lattice fabricated with 8wt% Au_{25} photoresist. (**E-G**) In-situ SEM compression of an octet lattice. (**H**) Engineering Stress-Engineering Strain curve for SP lattice fabricated with 8wt% Au_{25} photoresist. (**I-K**) In-situ SEM compression of an SP lattice.

We show that the nonlinear material response, high strength, and energy absorption of the printed nanocluster composite can be extended to complex 3D lattices. Octet lattices and Schwarz Primitive (SP) lattices (cite) are constructed and compressed in-situ. These structures show high energy absorption before densification. The increased stiffness in the material response suppresses the negative stiffness regions typically associated with layer-by-layer collapse of these lattices (*32*, *33*, *35*), which leads to their high absorption capabilities. Additionally, the octet lattice now fails at the nodes (Fig 3D-G) without buckling behavior that is

typically observed in polymeric octet lattices. Octet lattices relative densities of 19% and 27% and SP lattices with relative densities of 20% and 26% were mechanically tested in-situ. The octets have energy absorption capacities of 7.6 MJ/m^3 and 6.4 MJ/m^3 respectively and the SP lattices 7.3 MJ/m^3 and 9.7 MJ/m^3. Layer-by-layer collapse is observed only in the lower relative density SP lattice (Fig 3H-K) and suppressed in all other cases. Digital Image Correlation (DIC) is used to confirm the strain localization (Fig S11). Pillar compressions revealed the nanocluster resin fails at a high strength but at finite strain (~50%). They show a more brittle-like failure than typical polymer photoresists but gain a strain-hardening like behavior. This combination of properties is extendable to the lattice structures, enhancing their properties through suppression of negative stiffness while maintaining high recoverability (up to 80%).

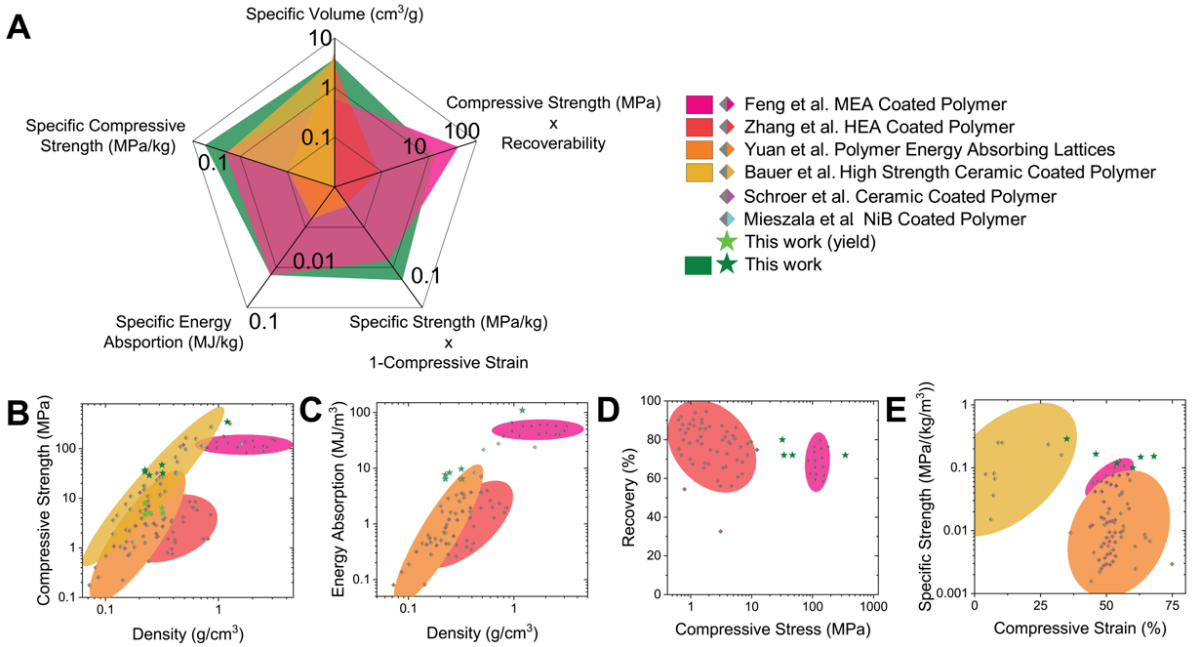

Fig. 4. Mechanical Performance of 3D Printed Nanocluster Polymer Nanolattices. (**A**) Sprider plot of mechanical properties of nanocluster composites compared to other polymer lattices. (**B**) Strength and (**C**) Absorbed energy vs. density of nanocluster composites compared to other polymer microlattices with inorganic coatings and bulk materials. (**D**) Recovery vs. compressive stress and **(E**) specific strength vs. compressive strain of our nanocluster polymer nanolattice and other lattices.

Fig. 4 compares the compressive strength, energy absorption, deformation, recovery, and density of the nanocluster composites to that of polymer micro- and nanolattices with inorganic coatings, as well as conventional material systems. The nanocluster composite pillars and nanolattices (Green Starsin Figure 4a) have comparably high specific strength to the state-of-the-

art polymer-coated microlattices. The energy absorption of our nanocluster composite octet and SP lattices are also among the best of any recoverable microlattice. It should be noted that we do not include glassy carbon structures in Fig. 4 as they are brittle ceramic materials which can only sustain high strains a single time. Our work provides a single step process which yields a highly recoverable lattice with outstanding impact resistance. Fig. 4C and D compares the recoverability vs strength vs strain of our nanocluster composite nanolattice with other state-of-the-art micro or nano lattices. Overall, our nanocluster nanolattice shows an unprecedented combination of high specific strength, high specific energy absorption, large deformability, and good recoverability (Fig. 4A). In addition, using the nanocluster-based photoresists, these properties can be achieved without the need for multiple post-processing steps such as the coating required for core-shell composite lattices.

Besides the superior printability and extraordinary mechanical performance, our framework also enables of the fabrication of complex nanoporous structures (Fig. 5). For example, the nanocluster composites were transformed into glassy carbon (confirmed by Raman analysis in Fig. S12) with complex nanoporous features through pyrolysis (heated to 900^{o}C) under argon flow. Fig. 5A-C shows a nanoporous cube (printed using 20 wt% $Ag_{28}Pt$ photoresist). The average pore size analyzed from Fig. 5B is ~56 ± 23 nm (Fig. S13), and the porosity of the surface layer is ~50%. The nanopores penetrate a layer ~500-700 nm into the structure (Fig. 5C), which is determined by the direct image of the cross-section of the structure after the FIB. Due to the penetration depth of the nanopores, two types of nanoporous structures can be obtained. As shown in Fig 5D, for the larger pillar with a diameter of ~ 8 um, it has graded porosity with a solid core surrounded by a nanoporous shell. For small pillars with a diameter less than 2 um (Fig 5E), the porosity is pervasive throughout the whole structure. Octet lattices were pyrolyzed to form structures with two levels of porosity: 1) geometrically designed spaces between lattice struts and 2) nanocluster-induced nanopores within lattice struts (Fig. 5F).

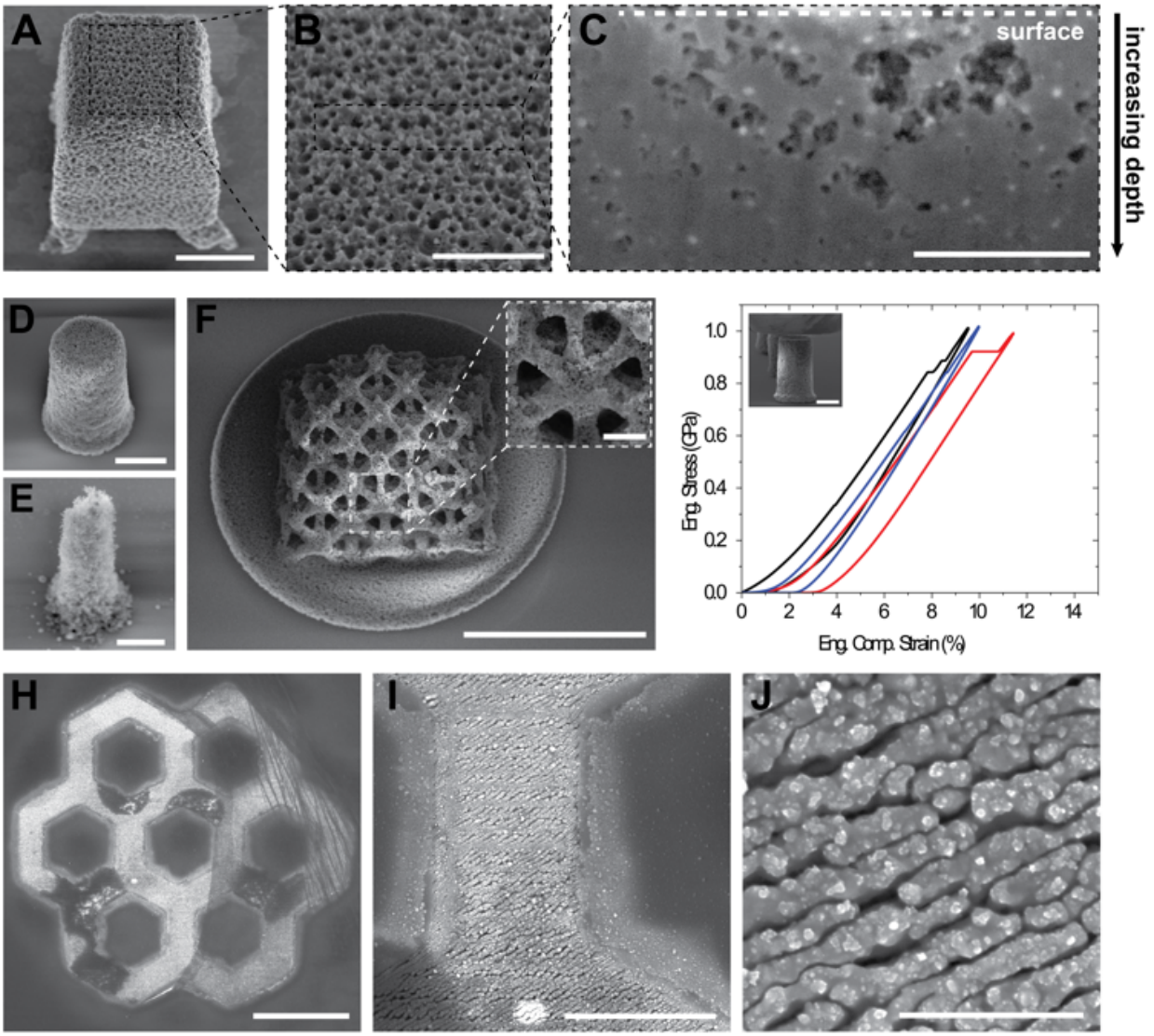

Fig. 5. Hierarchical, Tunable and Anisotropic Nanoporous Structures of Glassy Carbon (A-F) and Silk Protein (G-I). (**A**) Cube on supports with 50% porosity fabricated from 20 wt% $Ag_{28}Pt$ photoresist after pyrolysis at 900°C. (**B**) Magnified view of top surface. (**C**) Cross-section image of nanoporous cube (**D**) Big and (E)small nanoporous pillars fabricated from 10 wt% $Ag_{28}Pt$ photoresist after pyrolysis at 900°C. (**F**) Nanoporous octet lattice fabricated from 10 wt% $Ag_{28}Pt$ photoresist after pyrolysis at 900°C. (**G**) Compressive engineering stress-engineering strain curves of nanoporous pillars made using a 10 wt% $Ag_{28}Pt$ photoresist. Inset shows SEM image of nanoporous pillar with a density of 1.07 g/cm^3. (**H-J**) SEM images of silk fibroin honeycomb structures. Scale bars: (A), (B) 5 μm, (C) 2 μm, (D) 1 μm, (E) 10 μm, (inset) 2 μm, (F) 5 μm, (G) 10 μm, (H) 2 μm, (I) 200 nm.

The porosity of the "surface" layer can be tailored by the concentration of nanoclusters and the printed structures containing less nanoclusters resulted in less porosity after pyrolysis. (Fig. S14 and Fig. S15). Previous work involving pyrolysis of PETA-based photoresists resulted in glassy carbon without porosity (*11*, *44*). Here, we propose that the nanopores result from the melting of nanoclusters during pyrolysis. We suggest that, as the structure is heated to 900°C, the nanoclusters merge to form larger particles and eventually precipitate out of the structure. The melting temperature of 1-2 nm nanoclusters is estimated to be 600-900°C (*39*), which is consistent with the observation that no nanopores form at pyrolysis temperatures at 550°C (Fig S16). This is also supported by the observation of ~100-500 nm metal particles on the surface of some pyrolyzed structures, and the nearby substrate (Fig. S17). Energy-dispersive X-ray spectroscopy (EDS) confirmed the presence of Au or Ag in or on the pyrolyzed structures (Fig. S18).

Nanoporous glassy carbon pillars made using a 10 wt% $Ag_{28}Pt$ photoresist were mechanically tested via compression (Fig. 5G). These structures have a radius of 3.82 ± 0.04 μm, a height of 20.3 ± 0.6 μm. Pillars were printed on a ~1 μm thick, and ~20 μm wide platform to promote isotropic shrinkage in the pillar. The compressed pillars show several different material responses. A third of the samples have a smooth, linear stress-strain curve up to sudden fracture at ~15% strain. The shape of this stress-strain curve is similar to that of brittle materials. Other samples exhibit multiple slip events with small increases in slope after each slip event. In-situ experiments confirm that these slip events coincide with fracture of small parts of the porous material. (Fig. S19) These samples fail suddenly at a high stress of ~2 GPa. Other samples failed at low stresses of ~100 MPa. These samples may have failed by bending and breaking at the base of the pillar but are included here regardless. The average failure strength is 1.3 ± 0.9 GPa. Including the metal nanoclusters in the weight, the nanoporous pillars have a density of 1.07 g/cm^3, and a specific strength of 1.2 ± 0.8 GPa g^{-1} cm^3.The nanoporous pillars have comparable density (~1.07 g/cm^3) to glassy carbon nanolattices (~1 g/cm^3) (*13*), and similarly high strengths. This suggests that a stochastic porous structure with nanoscale size effects may approach the specific strength of an architected lattice with an optimized topology.

Nanoclusters were also used to print natural proteins. Currently, two-photon lithography-based 3D printing of protein structures is very slow, with reported speeds that are generally in the range of 1-1000 μm/s (*27*, *43*). Additionally, creating the hierarchical structures with

controllable anisotropic pores as observed in natural structural materials remains challenging. (*19*, *44*). The nanocluster-protein photoresist exploits the efficient singlet oxygen generation and significant photothermal effect of metal nanoclusters under excitation (*40*), which induce the photo-crosslinking of proteins through oxidization of the tyrosine residues (Fig. 1B), as well as the formation of directional β-sheet crystalline regions though local heating (*45*). Silk fibroin is used in the photoresist due to its high content of tyrosine (5.4%) distributed at the boundary of crystalline domains (*46*). A water-dispersible Au_{22} nanocluster was synthesized (*47*) and used in the photoresist.

Fibroin microstructures are printed at speeds up to 100 mm/s (laser power ~25 mW). This is much faster (about two orders of magnitude) than most of other photo-initiators for two-photon lithography of proteins under similar printing setups which are also based on the oxidation-induced photocrosslinking mechanism.(*27*, *43*) Furthermore, the printed protein structures are composed of aligned bundles (Fig. 5G-I) which indicate that directional self-assembly occurred during fabrication. Raman spectroscopy suggests the formation of many β-sheets (Fig. S20). These form aligned crystalline domains with nanoscale dimensions. The voids with ~10-50 nm in diameter which penetrate 200-300 nm (Fig. 21) in the printed structures may be due to the destruction of softer parts of the protein chains by the strong photothermal effect. Together, this leads to the formation of silk fibroin structures with anisotropic porosity.

In summary, we develop a class of nanocluster-based, highly sensitive photoresist for 3D nanoprinting. We fabricate nanocluster composite nanolattices and their derived structures with unprecedented structural complexity (*e.g.,* nanoporosity, hierarchy, anisotropy, gradience). We demonstrate the superior mechanical performance of nanocluster polymer nanolattices which exhibit an unprecedented combination of high specific energy absorption, high specific strength, large deformation, good recovery, and a strain hardening behavior. Looking forward, we envision that more mechanical metamaterials based on the nanocluster polymer nanolattices and their derived structures can be obtained through *i*) the combination of the hundreds of metal (including other inexpensive elements such as Cu) nanoclusters (*38*) with different types of monomers, and *ii*) the rational design of other 3D topologies, and *iii*) the optimization of the post treatment (e.g. heating and pyrolysis) conditions. In a broader sense, this work shows that it may be possible to use additional photoactive, multifunctional, and adaptable nanomaterials to

enhance the process and products of other scalable 3D nanoprinting (*2*, *8*) or additive manufacturing techniques such as stereolithography (*6*).

References

1. B. E. Kelly, I. Bhattacharya, H. Heidari, M. Shusteff, C. M. Spadaccini, H. K. Taylor, Volumetric additive manufacturing via tomographic reconstruction. *Science*. **363**, 1075–1079 (2019).
2. S. K. Saha, D. Wang, V. H. Nguyen, Y. Chang, J. S. Oakdale, S.-C. Chen, Scalable submicrometer additive manufacturing. *Science*. **366**, 105–109 (2019).
3. W. Jung, Y.-H. Jung, P. V. Pikhitsa, J. Feng, Y. Yang, M. Kim, H.-Y. Tsai, T. Tanaka, J. Shin, K.-Y. Kim, H. Choi, J. Rho, M. Choi, Three-dimensional nanoprinting via charged aerosol jets. *Nature*. **592**, 54–59 (2021).
4. S. Kawata, H.-B. Sun, T. Tanaka, K. Takada, Finer features for functional microdevices. *Nature*. **412**, 697–698 (2001).
5. D. A. Walker, J. L. Hedrick, C. A. Mirkin, Rapid, large-volume, thermally controlled 3D printing using a mobile liquid interface. *Science*. **366**, 360–364 (2019).
6. D. G. Moore, L. Barbera, K. Masania, A. R. Studart, Three-dimensional printing of multicomponent glasses using phase-separating resins. *Nature Materials*. **19**, 212–217 (2020).
7. X. Wen, B. Zhang, W. Wang, F. Ye, S. Yue, H. Guo, G. Gao, Y. Zhao, Q. Fang, C. Nguyen, X. Zhang, J. Bao, J. T. Robinson, P. M. Ajayan, J. Lou, 3D-printed silica with nanoscale resolution. *Nat. Mater.* **20**, 1506–1511 (2021).

8. V. Hahn, T. Messer, N. M. Bojanowski, E. R. Curticean, I. Wacker, R. R. Schröder, E. Blasco, M. Wegener, Two-step absorption instead of two-photon absorption in 3D nanoprinting. *Nat. Photon.* **15**, 932–938 (2021).
9. Z. C. Eckel, C. Zhou, J. H. Martin, A. J. Jacobsen, W. B. Carter, T. A. Schaedler, Additive manufacturing of polymer-derived ceramics. *Science*. **351**, 58–62 (2016).
10. J. Bauer, L. R. Meza, T. A. Schaedler, R. Schwaiger, X. Zheng, L. Valdevit, Nanolattices: An Emerging Class of Mechanical Metamaterials. *Advanced Materials*. **29**, 1701850 (2017).
11. Architectures down to nano. *Nat. Mater.* **20**, 1451–1451 (2021).
12. X. Zheng, W. Smith, J. Jackson, B. Moran, H. Cui, D. Chen, J. Ye, N. Fang, N. Rodriguez, T. Weisgraber, C. M. Spadaccini, Multiscale metallic metamaterials. *Nature Materials*. **15**, 1100–1106 (2016).
13. X. Zhang, A. Vyatskikh, H. Gao, J. R. Greer, X. Li, Lightweight, flaw-tolerant, and ultrastrong nanoarchitected carbon. *PNAS*. **116**, 6665–6672 (2019).
14. L. R. Meza, S. Das, J. R. Greer, Strong, lightweight, and recoverable three-dimensional ceramic nanolattices. *Science*. **345**, 1322–1326 (2014).
15. J. Ye, L. Liu, J. Oakdale, J. Lefebvre, S. Bhowmick, T. Voisin, J. D. Roehling, W. L. Smith, M. R. Cerón, J. van Ham, L. B. Bayu Aji, M. M. Biener, Y. M. Wang, P. R. Onck, J. Biener, Ultra-low-density digitally architected carbon with a strutted tube-in-tube structure. *Nat. Mater.* **20**, 1498–1505 (2021).
16. X. Zheng, H. Lee, T. H. Weisgraber, M. Shusteff, J. DeOtte, E. B. Duoss, J. D. Kuntz, M. M. Biener, Q. Ge, J. A. Jackson, S. O. Kucheyev, N. X. Fang, C. M. Spadaccini, Ultralight, ultrastiff mechanical metamaterials. *Science*. **344**, 1373–1377 (2014).

17. D. Behera, S. Chizari, L. A. Shaw, M. Porter, R. Hensleigh, Z. Xu, N. K. Roy, L. G. Connolly, X. (Rayne) Zheng, S. Saha, J. B. Hopkins, M. A. Cullinan, Current challenges and potential directions towards precision microscale additive manufacturing – Part II: Laser-based curing, heating, and trapping processes. *Precision Engineering*. **68**, 301–318 (2021).
18. M. Carlotti, V. Mattoli, Functional Materials for Two-Photon Polymerization in Microfabrication. *Small*. **15**, 1902687 (2019).
19. O. A. Tertuliano, J. R. Greer, The nanocomposite nature of bone drives its strength and damage resistance. *Nature Mater*. **15**, 1195–1202 (2016).
20. J. K. Hohmann, M. Renner, E. H. Waller, G. von Freymann, Three-Dimensional μ-Printing: An Enabling Technology. *Advanced Optical Materials*. **3**, 1488–1507 (2015).
21. J. Serbin, A. Egbert, A. Ostendorf, B. N. Chichkov, R. Houbertz, G. Domann, J. Schulz, C. Cronauer, L. Fröhlich, M. Popall, Femtosecond laser-induced two-photon polymerization of inorganic–organic hybrid materials for applications in photonics. *Opt. Lett., OL*. **28**, 301–303 (2003).
22. P. Kiefer, V. Hahn, M. Nardi, L. Yang, E. Blasco, C. Barner-Kowollik, M. Wegener, Sensitive Photoresists for Rapid Multiphoton 3D Laser Micro- and Nanoprinting. *Advanced Optical Materials*. **8**, 2000895 (2020).
23. W. Zhou, S. M. Kuebler, K. L. Braun, T. Yu, J. K. Cammack, C. K. Ober, J. W. Perry, S. R. Marder, An Efficient Two-Photon-Generated Photoacid Applied to Positive-Tone 3D Microfabrication. *Science*. **296**, 1106–1109 (2002).
24. L. Li, R. R. Gattass, E. Gershgoren, H. Hwang, J. T. Fourkas, Achieving λ/20 Resolution by One-Color Initiation and Deactivation of Polymerization. *Science*. **324**, 910–913 (2009).

25. I. Henning, A. W. Woodward, G. A. Rance, B. T. Paul, R. D. Wildman, D. J. Irvine, J. C. Moore, A Click Chemistry Strategy for the Synthesis of Efficient Photoinitiators for Two-Photon Polymerization. *Advanced Functional Materials*. **30**, 2006108 (2020).
26. T. Wloka, M. Gottschaldt, U. S. Schubert, From Light to Structure: Photo Initiators for Radical Two-Photon Polymerization. *Chemistry – A European Journal*. **28**, e202104191 (2022).
27. C. L. Lay, C. S. L. Koh, Y. H. Lee, G. C. Phan-Quang, H. Y. F. Sim, S. X. Leong, X. Han, I. Y. Phang, X. Y. Ling, Two-Photon-Assisted Polymerization and Reduction: Emerging Formulations and Applications. *ACS Appl. Mater. Interfaces*. **12**, 10061–10079 (2020).
28. M. Luitz, M. Lunzer, A. Goralczyk, M. Mader, S. Bhagwat, A. Warmbold, D. Helmer, F. Kotz, B. E. Rapp, High Resolution Patterning of an Organic–Inorganic Photoresin for the Fabrication of Platinum Microstructures. *Advanced Materials*. **33**, 2101992 (2021).
29. S. K. Saha, B. Au, J. S. Oakdale, High-Speed Direct Laser Writing of Silver Nanostructures via Two-Photon Reduction. *Advanced Engineering Materials*. **21**, 1900583 (2019).
30. C. M. Spadaccini, "Chapter 13.4 - Future perspectives on materials for two-photon polymerization" in *Three-Dimensional Microfabrication Using Two-Photon Polymerization (Second Edition)*, T. Baldacchini, Ed. (William Andrew Publishing, 2020; https://www.sciencedirect.com/science/article/pii/B9780128178270000618), *Micro and Nano Technologies*, pp. 671–681.
31. J. Bauer, S. Hengsbach, I. Tesari, R. Schwaiger, O. Kraft, High-strength cellular ceramic composites with 3D microarchitecture. *PNAS*. **111**, 2453–2458 (2014).

32. X. Zhang, J. Yao, B. Liu, J. Yan, L. Lu, Y. Li, H. Gao, X. Li, Three-Dimensional High-Entropy Alloy–Polymer Composite Nanolattices That Overcome the Strength–Recoverability Trade-off. *Nano Lett.* **18**, 4247–4256 (2018).

33. M. Mieszala, M. Hasegawa, G. Guillonneau, J. Bauer, R. Raghavan, C. Frantz, O. Kraft, S. Mischler, J. Michler, L. Philippe, Micromechanics of Amorphous Metal/Polymer Hybrid Structures with 3D Cellular Architectures: Size Effects, Buckling Behavior, and Energy Absorption Capability. *Small*. **13**, 1602514 (2017).

34. A. Schroer, J. M. Wheeler, R. Schwaiger, Deformation behavior and energy absorption capability of polymer and ceramic-polymer composite microlattices under cyclic loading. *Journal of Materials Research*. **33**, 274–289 (2018).

35. X. Feng, J. U. Surjadi, R. Fan, X. Li, W. Zhou, S. Zhao, Y. Lu, Microalloyed medium-entropy alloy (MEA) composite nanolattices with ultrahigh toughness and cyclability. *Materials Today*. **42**, 10–16 (2021).

36. L. Cheng, T. Tang, H. Yang, F. Hao, G. Wu, F. Lyu, Y. Bu, Y. Zhao, Y. Zhao, G. Liu, X. Cheng, J. Lu, The Twisting of Dome-Like Metamaterial from Brittle to Ductile. *Advanced Science*. **8**, 2002701 (2021).

37. D. W. Abueidda, M. Elhebeary, C.-S. (Andrew) Shiang, R. K. Abu Al-Rub, I. M. Jasiuk, Compression and buckling of microarchitectured Neovius-lattice. *Extreme Mechanics Letters*. **37**, 100688 (2020).

38. R. Jin, C. Zeng, M. Zhou, Y. Chen, Atomically Precise Colloidal Metal Nanoclusters and Nanoparticles: Fundamentals and Opportunities. *Chem. Rev.* **116**, 10346–10413 (2016).

39. F. Gao, Z. Gu, "Melting Temperature of Metallic Nanoparticles" in *Handbook of Nanoparticles*, M. Aliofkhazraei, Ed. (Springer International Publishing, Cham, 2016; https://doi.org/10.1007/978-3-319-15338-4_6), pp. 661–690.

40. Y. Xie, W. Zheng, X. Jiang, Near-Infrared Light-Activated Phototherapy by Gold Nanoclusters for Dispersing Biofilms. *ACS Appl. Mater. Interfaces*. **12**, 9041–9049 (2020).

41. X. Lin, C. Liu, K. Sun, R. Wu, X. Fu, J. Huang, Structural isomer and high-yield of Pt1Ag28 nanocluster via one-pot chemical wet method. *Nano Res.* **12**, 309–314 (2019).

42. Q. Li, C. J. Zeman, Z. Ma, G. C. Schatz, X. W. Gu, Bright NIR-II Photoluminescence in Rod-Shaped Icosahedral Gold Nanoclusters. *Small*. **17**, 2007992 (2021).

43. D. Serien, K. Sugioka, Fabrication of three-dimensional proteinaceous micro- and nano-structures by femtosecond laser cross-linking. *OEA*. **1**, 180008-180008–18 (2018).

44. F. Libonati, G. X. Gu, Z. Qin, L. Vergani, M. J. Buehler, Bone-Inspired Materials by Design: Toughness Amplification Observed Using 3D Printing and Testing. *Advanced Engineering Materials*. **18**, 1354–1363 (2016).

45. Y. Xiao, Y. Liu, W. Zhang, P. Qi, J. Ren, Y. Pei, S. Ling, Formation, Structure, and Mechanical Performance of Silk Nanofibrils Produced by Heat-Induced Self-Assembly. *Macromolecular Rapid Communications*. **42**, 2000435 (2021).

46. X. Mu, J. K. Sahoo, P. Cebe, D. L. Kaplan, Photo-Crosslinked Silk Fibroin for 3D Printing. *Polymers*. **12**, 2936 (2020).

47. K. Pyo, V. D. Thanthirige, K. Kwak, P. Pandurangan, G. Ramakrishna, D. Lee, Ultrabright Luminescence from Gold Nanoclusters: Rigidifying the Au(I)–Thiolate Shell. *J. Am. Chem. Soc.* **137**, 8244–8250 (2015).

Acknowledgements: This work was financially supported by the National Science Foundation (CMMI-2052251 and DMR-2002936/2002891), and the American Chemical Society Petroleum Research Doctoral New Investigator Grant. D.D. acknowledges the National Science Foundation Graduate Research Fellowship under Grant No. 1656518. J.K. was supported by a Stanford Graduate Fellowship. Part of this work was performed at the Stanford Nano Shared Facilities (SNSF) and Stanford Nanofabrication Facility (SNF), which are supported by the National Science Foundation under award ECCS-1542152.

Author contributions: Q.L. conceived the idea of the nanocluster-based photoresist. X.W.G. and Q.L. designed the research. J.K., D.D. and Q.L. performed the 3D printing. J.K. conducted the mechanical test. D.D. and O.T. performed the structure characterization. C.J.Z. and G.C.S. performed simulations. Q.L., J.K., D.D., O.T. and X.W.G. wrote the paper and all authors commented on it.

Competing interests: The authors declare no competing interests.

Supplementary Materials

Materials and Methods

Figs. S1 to S16

References (*21,32,33,53*)